Al-Al_2O_3-Al Tunnel-Junction-Array Coulomb Blockade Thermometers

Lihong Hu (胡利洪)[1,2], Junya Feng (冯军雅)[1,2], Lei Xu (徐磊)[1,2], Xinyi Zheng (郑新义)[1,2], Sicheng Zhou (周思成)[1,2], Siyuan Zhou (周思远)[1,2], Ximing Zhang (张栖铭)[1,2], Zishuo Peng (彭孜硕)[1,2], Xiaohui Song (宋小会)[1,2,3], Zhaozheng Lyu (吕昭征)[1,2], Ziwei Dou (窦子威)[1,2], Jie Shen (沈洁)[1,2,3], Peiling Li (李沛岭)[1,2,3], Fanming Qu (屈凡明)[1,2,3], Guangtong Liu (刘广同)[1,2,3†] and Li Lu (吕力)[1,2,3]

[1]Beijing National Laboratory for Condensed Matter Physics, Institute of Physics, Chinese Academy of Sciences, Beijing 100190, China
[2]School of Physical Sciences, University of Chinese Academy of Sciences, Beijing 100049, China
[3]Hefei National Laboratory, Hefei, Anhui 230088, China

Reliable electron thermometry is essential for millikelvin quantum-transport experiments, where weak electron–phonon coupling makes the electron temperature highly susceptible to residual heat loads. We report Al − Al_2O_3 − Al tunnel-junction-array Coulomb blockade thermometers (CBTs) that enable wide-range, on-chip electron thermometry compatible with high magnetic fields. The fabricated multi-junction devices exhibit well-defined Coulomb-blockade conductance dips, an enhanced operating voltage range, and robust performance in magnetic fields up to 10 T after the Al electrodes are driven into the normal state. By combining measurements from distinct CBT devices optimized with different charging energies and thermalization structures, we demonstrate reliable electron thermometry over a broad temperature range from approximately 30 mK to 3 K. The observed saturation of the electron temperature at the lowest temperatures indicates residual electron overheating, highlighting thermalization and parasitic-heat control as the key constraints for millikelvin thermometry. These results demonstrate that Al − Al_2O_3 − Al CBT arrays constitute a practical and reliable platform for wide-range, magnetic-field-compatible on-chip electron thermometry, with broad applications in mesoscopic physics, quantum-material research, and cryogenic metrology.

Keywords: Coulomb blockade thermometer; electron thermometry; electron overheating; millikelvin instrumentation
PACS: 07.20.Dt, 73.23.Hk, 85.35.Gv, 72.10.Di

1. Introduction

Accurate determination of the electron temperature is a prerequisite for low-temperature quantum transport experiments. In mesoscopic and superconducting devices, the measured electrical characteristics are governed by the electron temperature rather than the temperature of the cryostat[1–3]. Below a few hundred millikelvin, the electron–phonon coupling decreases rapidly, causing the electron subsystem to decouple from the lattice[4]. Consequently, even minute residual heat loads originating from radio-frequency noise, measurement-induced dissipation, insufficient filtering, or imperfect thermal anchoring can drive the electron temperature significantly above the refrigerator temperature. Under these conditions, a thermometer mounted on the mixing chamber or ^{3}He pot no longer provides an accurate measure of the local electron temperature.

Among various cryogenic thermometry techniques, Coulomb blockade thermometry (CBT) has emerged as one of the most reliable methods for primary electron thermometry[1,3,5–8]. A CBT consists of an array of metallic islands connected by tunnel junctions. Around zero dc bias, the differential conductance is suppressed by the single-electron charging effects, leading to a characteristic Coulomb-blockade conductance dip. In the weak Coulomb-blockade regime, the conductance profile depends only on the ratio of the charging energy to k_BT, enabling the electron temperature to be determined directly from the full conductance curve and the full width at half minimum of the conductance dip without calibration[5,9,10]. Furthermore, CBTs are naturally compatible with on-chip integration because they are lithographically defined metallic tunnel-junction arrays that can be placed in close proximity to mesoscopic devices. Since their thermometric response arises from single-electron tunnelling and Coulomb blockade rather than superconductivity, they remain functional in high magnetic fields once the Al electrodes are driven into the normal state. Recent developments have extended CBTs to radio-frequency readout, gate-defined architectures for microkelvin thermometry, and membrane-based nanocalorimetry for high-field measurements[11–13].

Despite these advantages, extending CBT operation to the millikelvin regime remains challenging, primarily because of electron overheating. The electron–phonon cooling power collapses approximately as T^5 [14], making the electron temperature extremely sensitive to parasitic heat leaks at ultralow temperatures. Recent studies have demonstrated that achieving electron temperatures in the few-millikelvin range requires careful optimization of the thermalization architecture, including large normal-metal cooling volumes, efficient microwave filtering, and low-noise measurement circuitry[7,12,15–17]. These considerations highlight that wide-range CBT thermometry is as much a device-engineering challenge as a primary-thermometry problem: the charging energy, tunnel resistance and on-chip thermalization must be optimized together for the intended temperature window.

In this work, we develop a series of Al − Al_2O_3 − Al tunnel-junction-array CBTs for wide-range on-chip electron thermometry. A reproducible fabrication process is established to produce highly uniform tunnel junctions with well-controlled electrical characteristics. We systematically investigate the characteristic thermometric response of the CBTs, demonstrate the advantages of the multi-junction-array architecture, and evaluate device operation in magnetic fields up to 10 T. By comparing devices with different junction areas and on-chip thermalization structures, we further elucidate the influence of electron overheating on thermometric accuracy and identify effective approaches for suppressing electron-temperature saturation at low temperatures. By combining CBT devices individually optimized for complementary temperature regimes, we achieve reliable on-chip electron thermometry over a collective temperature range from 30 mK to 3 K. This ensemble of devices provides a practical and robust platform for primary electron thermometry in low-temperature, high-magnetic-field transport experiments on mesoscopic and quantum-material systems, as well as for applications in cryogenic metrology.

2. Coulomb blockade thermometry principle and analysis protocol

For a uniform CBT array containing N tunnel junctions connected in series, the normalized differential conductance in the

†Corresponding author. gtliu@iphy.ac.cn

weak-blockade regime ($u_N \ll 1$) is given by [5,9,10]

$$\frac{G(V)}{G_T} = 1 - u_N g(v_N), \tag{1}$$

where G_T is the asymptotic high-bias conductance, $u_N = E_C/(k_B T)$ and $v_N = eV/(Nk_B T)$. Here, $E_C = [(N-1)/N]e^2/C_\Sigma$ is the effective charging energy of the system, C_Σ is the total capacitance of each metallic island, V is the total voltage across the series array, and T is the electron temperature. The universal conductance function is

$$g(x) = \frac{x \sinh x - 4\sinh^2(x/2)}{8\sinh^4(x/2)} \tag{2}$$

which yields $g(0) = 1/6$ at zero bias. Consequently, the normalized zero-bias conductance-dip depth is

$$\Delta G/G_T = (G_T - G_0)/G_T \approx u_N/6 \tag{3}$$

where G_0 denotes the zero-bias conductance. Another important primary thermometric quantity is the full width at half minimum (FWHM) of the conductance dip,

$$V_{1/2} \simeq 5.439\frac{Nk_B T}{e} \tag{4}$$

which is independent of both the absolute tunnel resistance and the charging energy in the strict weak-blockade limit [5,9]. When u_N is no longer much smaller than unity, higher-order finite-charging-energy corrections become important. In this regime, the normalized zero-bias conductance dip can be expanded as [6,18]

$$\Delta G/G_T \approx u_N/6 - {u_N}^2/60 + {u_N}^3/630 \tag{5}$$

These analytical expressions provide convenient estimates of the electron temperature. In practice, however, higher accuracy is achieved by numerically calculating the complete differential conductance using the orthodox single-electron tunnelling theory [5,19,20]. In this work, the full tunnelling model is employed to determine the device parameters, including the total island capacitance C_Σ and the asymptotic conductance G_T, from reference measurements. These calibrated parameters are then fixed for the analysis of all temperature-dependent conductance data. To reduce the computational complexity of multi-junction arrays, the series array is mapped onto an equivalent double-junction system within the orthodox tunnelling formalism. Although this approach eliminates the limitations of the analytical weak-blockade approximation, it still assumes a uniform array and therefore does not explicitly include the full distribution of individual junction resistances R_i and capacitances C_i.

Electron overheating was incorporated using a steady-state heat-balance model for the island electron temperature T_e. In this model, the Joule power and residual parasitic heat load are balanced by electron–phonon cooling [7,14,21,22],

$$V^2 G_T + P_0 = \Sigma\Omega\left(T_e^5 - T_p^5\right) \tag{6}$$

where $V^2 G_T$ is the Joule power dissipated in the tunnel-junction array, P_0 represents the residual heat load, Σ is the electron–phonon coupling constant, Ω is the effective metallic volume, and T_p is the phonon temperature. The resulting bias-dependent electron temperature $T_e(V)$ is then used self-consistently in the tunnelling model to generate the corresponding differential conductance. In the absence of parasitic heating and under zero-bias conditions, the minimum electron temperature approaches the phonon temperature, $T_e^{min} \simeq T_p$. Representative literature values of the electron–phonon coupling constant are $\Sigma_{Al} \approx 0.2 \times 10^9$ Wm^{-3}K^{-5} for Al and $\Sigma_{Au} \approx 2.4 \times 10^9$ Wm^{-3}K^{-5} for Au [4]. The nominal metallic volume was estimated from the measured dimensions of the thermalization pads and the deposited film thickness, assuming that the entire pad participates in electron–phonon energy relaxation. The residual heat load P_0 was estimated from the saturation of the CBT electron temperature at the lowest bath temperature. The charging energy E_C and asymptotic conductance G_T were first determined from higher-temperature conductance traces, where electron overheating was negligible, and were subsequently fixed in the low-temperature analysis. The lowest-temperature conductance trace was then fitted using the full master-equation model to obtain the saturated zero-bias electron temperature $T_{e,sat}$. At zero dc bias, the dc Joule-heating contribution vanishes, and the heat-balance equation reduces to

$$P_0 = \Sigma\Omega\left(T_{e,sat}^5 - T_{p,min}^5\right) \tag{7}$$

where $T_{p,min}$ is the lowest measured phonon temperature. Because this estimate relies on a single low-temperature data point, a literature value of Σ, and the nominal thermally active volume Ω, P_0 is reported as an effective, model-dependent estimate rather than an independently determined microscopic heat leak.

3. Results and discussion

3.1. Reproducible Al-Al_2O_3-Al tunnel-junction fabrication and junction uniformity

The $Al - Al_2O_3 - Al$ tunnel junctions were fabricated on Si/SiO_2 substrates using electron-beam lithography (EBL) followed by double-angle shadow evaporation. A bilayer MMA/PMMA resist stack was employed to form the undercut profile required for the Dolan-bridge-type process. After deposition of the first Al layer, an Al_2O_3 tunnel barrier was formed by *in situ* thermal oxidation, followed by deposition of the counter-electrode at the opposite evaporation angle. This fabrication process provides a clean overlap geometry with excellent reproducibility [23].

The tunnel resistance was controlled using a constant-flow oxidation protocol. Oxygen was introduced at a fixed flow rate of 3 sccm, and the oxidation was terminated when the chamber pressure reached a prescribed value. As shown in Fig. 1(a), the junction resistance-area product increases monotonically with the final oxidation pressure and saturates at approximately 8.5 k$\Omega \cdot \mu$m^2. This behavior provides a convenient means of tailoring the tunnel resistance through the combined optimization of the junction area and oxidation conditions.

For CBT devices operating below 100 mK, the junction capacitance is commonly increased to reduce the charging energy and thereby maintain operation in the weak or intermediate Coulomb-blockade regime. Increasing the junction area, however, simultaneously lowers the resistance of each tunnel junction, which may become comparable to or even smaller than the resistance quantum $R_K = h/e^2$. In this low-impedance regime, quantum charge fluctuations across individual junctions are significantly enhanced, leading to a pronounced renormalization and partial suppression of the Coulomb blockade. An effective solution is to employ a series array of tunnel junctions [10,24,25]. The increased total impedance of the array, together with the

Table 1. Resistance values of eight representative tunnel junctions and their deviations from the average resistance.

Junction number	1	2	3	4	5	6	7	8
R_i(kΩ)	3.48	3.50	3.51	3.36	3.58	3.47	3.44	3.61
$R_i - \overline{R}$(kΩ)	-0.014	0.006	0.016	-0.133	0.086	-0.023	-0.053	0.116

collective charging effects associated with multiple metallic islands, allows a well-defined and experimentally resolvable CBT conductance dip to persist even when the resistance of each individual junction is below R_K.

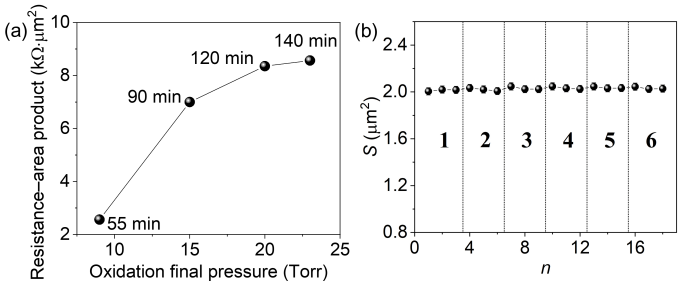


Fig. 1. Oxidation calibration and junction uniformity of $Al - Al_2O_3 - Al$ tunnel junctions. (a) Junction resistance–area product as a function of the final oxidation pressure at a fixed oxygen flow rate of 3 sccm. The numbers beside the data points indicate the oxidation time required to reach the corresponding pressure. (b) Distribution of the measured junction areas in the 10×6 test tunnel-junction array. The measured junction areas are narrowly distributed around the nominal value of 2 μm^2, demonstrating the excellent reproducibility of the lithography and double-angle shadow-evaporation processes. The numbers indicate the corresponding column indices in the array.

Junction uniformity is another critical factor determining the accuracy of Coulomb blockade thermometry [26]. Variations in junction resistance or capacitance give rise to nonuniform local charging energies and voltage distributions across the array, which results in broadening of the conductance dip and systematic errors in the extracted temperature. These effects become increasingly significant in the intermediate Coulomb-blockade regime, $u_N = E_C/k_BT \simeq 1$, where the conductance profile is particularly sensitive to the distributions of the individual junction resistances R_i and capacitances C_i. High junction uniformity is therefore essential for achieving accurate primary thermometry and extending the operation range of CBTs into the sub-100 mK temperature regime [26,27].

To evaluate the reproducibility of the fabrication process, a 10×6 test array was fabricated, consisting of ten tunnel junctions connected in series and six such branches connected in parallel. We first randomly selected 18 junctions and quantified their junction areas. As shown in Fig. 1(b), the measured junction areas are narrowly distributed around the designed value of 2 μm^2, with a variation of approximately 2%, indicating excellent uniformity in both the lithographic and shadow-evaporation processes. In addition, the resistances of eight randomly selected junctions are all centered around 3.5 kΩ, as summarized in Table 1. These results further demonstrate the high reproducibility of the electron-beam lithography, double-angle evaporation, and *in situ* oxidation processes.

3.2. Basic characterization and magnetic-field robustness of the CBT sensor

We first characterized the electrical response of the fabricated CBT devices. The schematic architecture of the series tunnel-junction array is shown in Fig. 2(a), and the differential-conductance (dI/dV) measurement configuration is illustrated in Fig. 2(b). Throughout this work, all low-temperature measurements were performed under magnetic fields exceeding the critical field of the Al electrodes, ensuring that the electrodes remained in the normal state. As shown in Figs. 2(c) and (d), a pronounced conductance dip centered near zero bias is clearly observed, which is the characteristic signature of Coulomb blockade in the tunnel-junction array.

To illustrate the advantage of the array configuration, we compared the differential-conductance characteristics of devices containing two junctions, ten junctions, and a 40×10 junction array, all measured at the same bath temperature of 300 mK [Fig. 2(c)]. As the number of series junctions increases, the Coulomb-blockade conductance dip becomes progressively broader in voltage and is more clearly resolved. This behavior arises because the characteristic voltage scale of the conductance dip increases approximately linearly with the number of junctions connected in series. Consequently, the voltage-dependent temperature response is effectively amplified, while the influence of local parameter variations and statistical fluctuations of individual junctions is reduced. As a result, the multi-junction array exhibits a substantially improved signal-to-noise ratio and provides higher thermometric resolution than devices containing only a few junctions. These results demonstrate that large series arrays are more suitable for accurate Coulomb blockade thermometry. It should be noted that the measured conductance traces exhibit a small residual voltage offset along the nominal bias axis, such that the conductance minimum does not always occur exactly at $V_{bias} = 0$. We attribute this displacement primarily to a residual dc voltage offset in the measurement circuit, with possible contributions from thermoelectric voltages generated along the cryogenic wiring, the zero offset of the dc bias source, and the input-offset voltage of the room-temperature transimpedance amplifier. The essentially rigid displacement of the conductance curves, without a resolvable systematic distortion of the conductance-dip line shape, is consistent with this interpretation. Before performing the full master-equation analysis, the conductance data within a narrow voltage window around the dip minimum were fitted to the quadratic form $G(V) = G_{min} + a(V - V_{off})^2$, allowing the offset voltage V_{off} to be determined independently for each trace. The effective device bias was then defined as $V_{eff} = V_{bias} - V_{off}$, and all temperature-dependent fits were performed as a function of V_{eff}. This procedure aligns the experimentally determined conductance minimum with the theoretical zero-bias point. Because this correction corresponds solely to a rigid horizontal translation of the conductance curve, it leaves both the conductance-dip depth and the full width at half minimum unchanged.

The magnetic-field robustness of the CBT response was fur-

ther investigated at a bath temperature of 300 mK. As shown in Fig. 2(d), the differential-conductance curves measured under magnetic fields from 2 to 10 T almost completely overlap once the Al electrodes are driven into the normal state. Within the experimental resolution, neither the depth nor the full width at half minimum of the conductance dip exhibits any systematic dependence on magnetic field. This magnetic-field independence behavior reflects the purely electrostatic origin of the Coulomb-blockade effect and confirms that the thermometric characteristics of the CBT are essentially unaffected by external magnetic fields. The excellent field robustness demonstrates that the fabricated Al-Al_2O_3-Al tunnel-junction array provides a reliable on-chip primary electron thermometer for mesoscopic transport experiments under high magnetic fields.

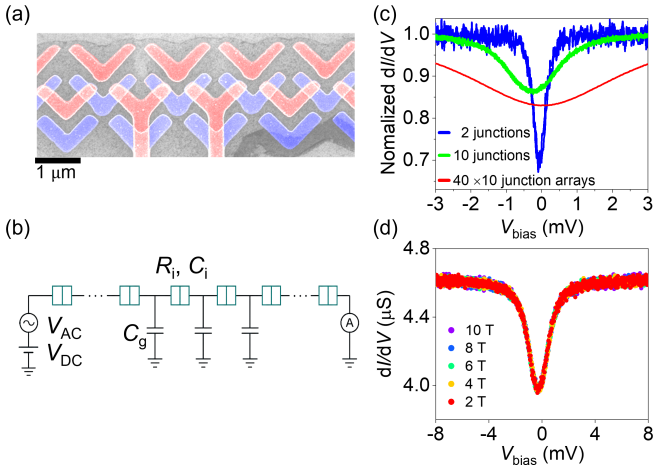


Fig. 2. Basic characterization of the CBT devices. (a) False-color scanning electron microscope (SEM) image of an Al – Al_2O_3 – Al tunnel-junction array. (b) Schematic of the differential-conductance measurement configuration. Each tunnel junction is characterized by a resistance R_i and capacitance C_i, while each metallic island is coupled to ground through a stray capacitance C_g. (c) Differential conductance (dI/dV) as a function of bias voltage for CBT devices containing different numbers of series junctions, measured at 300 mK. The conductance dip becomes broader and better resolved with increasing junction number. (d) $dI/dV - V_{bias}$ curves measured at 300 mK under magnetic fields from 2 to 10 T, demonstrating the magnetic-field robustness of the Coulomb-blockade response.

3.3. Temperature response of the multi-junction CBT array

After verifying the basic characteristics of the CBT devices, we fabricated device #D1 and evaluated its thermometric performance in a ^{3}He cryostat. Device #D1 consists of a 40×10 Al – Al_2O_3 – Al tunnel-junction array with a junction area of approximately 0.09 μm^2 and a single-junction resistance of about 75 kΩ. Representative temperature-dependent differential-conductance curves are shown in Fig. 3(a). As the temperature is lowered, the zero-bias conductance dip becomes progressively deeper and narrower, exhibiting the characteristic response of a Coulomb blockade thermometer.

The experimental conductance curves were analyzed using the full master-equation model described in Section 2, which includes the influence of bias-induced Joule heating. The corresponding numerical fits are shown as solid lines in Fig. 3(a), yielding a charging energy of $E_C/k_B \simeq 157$ mK. The measured conductance curves are well reproduced over most of the investigated temperature range by the CBT model, whereas systematic deviations become apparent at 250 mK. Such deviations are expected as the normalized charging energy $u_N = E_C/k_BT$ is no longer negligibly small and the device enters the intermediate-blockade regime, where the conductance profile becomes increasingly sensitive to junction nonuniformity, residual electron overheating, finite ac excitation, and background conductance. Consequently, maintaining a relatively small u_N within the target temperature range is important for achieving accurate CBT thermometry.

Within the weak Coulomb blockade regime, the temperatures extracted from the CBT agree well with those measured by the reference thermometer. As shown in the inset of Fig. 3(a), the relative deviation between the fitted CBT temperature and the ^{3}He refrigerator temperature remains below 1% at high temperatures and gradually increases upon cooling, reaching approximately 8% at $T = 250$ mK. The agreement in the weak Coulomb blockade regime confirms the accuracy and reliability of CBT thermometry. We further extracted the electron temperature using three analysis approaches: full master-equation fitting (T_{CBT}), the full-width-at-half-minimum method ($T_{V_{1/2}}$), and the conductance-dip method (T_{dip}), as summarized in Fig. 3(b). The temperatures obtained from these methods agree closely over the entire measurement range. This consistency indicates that, once E_C and G_T have been determined from the full conductance curve, the CBT can subsequently be operated in a rapid-readout mode by monitoring only the zero-bias conductance dip, thereby enabling efficient real-time temperature monitoring.

To extend the operating range of CBT towards lower temperatures, the effective charging energy should be reduced so that the device remains in the appropriate weak Coulomb blockade regime over the target temperature range. We therefore fabricated device #D2 with larger tunnel junctions. The device consists of 12 tunnel junctions connected in series, each with an area of 0.5 μm × 1.1 μm. The increased junction area enhances the junction capacitance, thereby reducing the charging energy E_C and improving the suitability of the device for low-temperature operation. Meanwhile, the larger junction geometry increases the metallic volume of the islands, enhancing both the electronic heat capacity and heat diffusion, which are beneficial for electron thermalization.

Device #D2 was characterized in a TL-400 dilution refrigerator, and the measured differential-conductance curves are shown in Fig. 3(c). The experimental data are well reproduced by the numerical calculations down to the onset of conductance saturation, indicating that device #D2 exhibits an extended low-temperature operating range compared with device #D1. However, as shown in the inset of Fig. 3(c), the conductance curves begin to saturate below approximately 100 mK. This behavior originates from progressive weakening of electron–phonon coupling at ultralow temperatures, which prevents the electron temperature of the metallic islands from following the lattice temperature. Consequently, further optimization of electron thermalization, such as increasing the metallic island volume, improving thermal anchoring, or enhancing microwave filtering, is required to extend CBT thermometry to even lower temperatures.

To further suppress electron overheating, we fabricated two 50×10 CBT array devices, #D3 and #D4, incorporating additional metallic thermalization structures to improve heat dissipation from the tunnel-junction islands. Device #D3 was fabricated with junction parameters similar to those of device

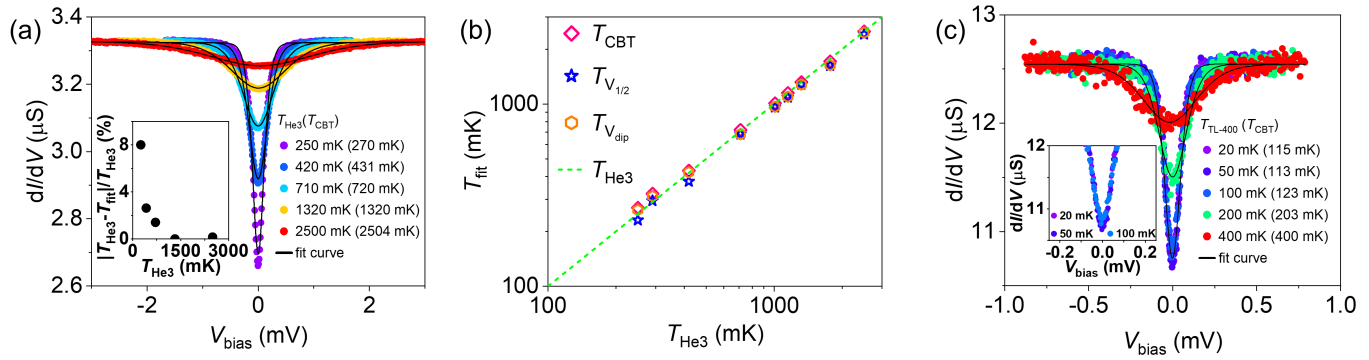


Fig. 3. Temperature response of the CBT devices. (a) Differential conductance of device #D1 measured at different temperatures. Black solid lines are full master-equation fits. The inset shows the relative difference between the extracted CBT temperature T_{CBT} and the RuO_2-thermometer temperature T_{He3} of the ^{3}He cryostat. (b) Comparison of temperatures obtained from full-curve fitting, the FWHM method and the conductance-dip method, labelled T_{CBT}, $T_{V_{1/2}}$ and T_{dip}, respectively, against T_{He3}. (c) Differential conductance of device #D2 measured at different temperatures, showing conductance saturation below ~ 100 mK. The inset shows an enlarged view of the saturated low-temperature curves.

#D2, while an Al metallic pad with dimensions of 50 μm × 20 μm × 100 nm was integrated adjacent to the junction array, as shown in Fig. 4(a). The temperature-dependent differential-conductance curves of device #D3 are shown in Fig. 4(b), yielding a fitted charging energy of $E_C/k_B \approx 23.4$ mK. As evidenced by the nearly overlapping low-temperature conductance curves in Fig. 4(d), the extracted electron temperature of device #D3 exhibits noticeable saturation only below approximately 42 mK, demonstrating a substantial improvement over device #D2. These results demonstrate that increasing the metallic volume and introducing an additional heat-diffusion pathway effectively enhance electron thermalization and significantly suppress electron overheating at ultralow temperatures.

To further extend the operating range towards lower temperatures, device #D4 was optimized by simultaneously reducing the charging energy and enhancing electron thermalization. The area of each tunnel junction was increased to 1 μm × 2 μm, thereby increasing the junction capacitance and reducing the charging energy. Meanwhile, the previous Al thermalization structure was replaced by Au thermalization electrodes with dimensions of 20 μm × 50 μm × 500 nm. Owing to its high electronic thermal conductivity and large electronic heat capacity, Au provides a more efficient thermalization pathway for the electrons in the metallic islands. The differential-conductance curves of the optimized device are shown in Fig. 4(c), yielding a fitted charging energy of $E_C/k_B \approx 15$ mK. As indicated by the low-temperature curves in Fig. 4(e), the onset of electron-temperature saturation is further suppressed to below 30 mK. However, the reduced charging energy of device #D4 also weakens the Coulomb blockade effect at elevated temperatures. Consequently, the conductance dip becomes nearly indiscernible above 300 mK, which limits accurate calibration in the higher-temperature regime.

For devices #D3 and #D4, the temperatures extracted from the CBT were further compared with those measured by the reference thermometer in the TL-400 dilution refrigerator. As shown in the insets of Figs. 4(b) and 4(c), the relative deviation remains below 2% throughout the high temperature weak Coulomb blockade regime, where $u_N = E_C/k_BT \ll 1$. The systematic improvement from devices #D2 to #D4 demonstrates that the ultimate low-temperature performance of $Al - Al_2O_3 - Al$ CBT sensors is determined not only by the charging energy, but also critically by the efficiency of electron thermalization. This conclusion is consistent with previous studies in the low-millikelvin regime, which have shown that large-volume normal-metal thermalization structures and minimized parasitic heat loads are essential for suppressing electron overheating and achieving accurate primary thermometry [7,15–17].

It should be emphasized that the observed low-temperature saturation does not indicate a breakdown of the CBT operating principle. Instead, it reflects the saturation of the electron temperature within the metallic islands. At ultralow temperatures, the electron-phonon coupling becomes too weak to dissipate the residual heat deposited in the electronic system, causing the electron temperature T_e to remain higher than the phonon bath temperature T_p. Under these conditions, even an extremely small parasitic heat load can lead to pronounced electron overheating. Therefore, increasing the effective metallic volume, improving thermal anchoring, reducing the measurement excitation power, and suppressing radio-frequency noise are all essential for extending CBT operation to lower temperatures.

To quantify the residual heating, we estimated the effective residual heat load P_0 on a per-island basis for devices #D3 and #D4 using Eq. (7) and the lowest-temperature data. The resulting values are approximately 1.9 fW per island for #D3 and 18 fW per island for #D4. The value obtained for #D3 is higher than the exceptionally low heat leaks achieved in highly optimized nuclear-demagnetization experiments, but remains within the broad range reported for metallic CBTs [7,16,28,29]. Each 50 × 10 array comprises ten parallel branches of 50 series junctions and therefore contains $10 \times (50 - 1) = 490$ internal islands, yielding nominal total residual heat loads of approximately 0.94 pW and 8.7 pW, respectively. Because the thermalization pads dominate the metallic volume, Ω was approximated by the pad volume, with the junction-electrode volume neglected. The larger nominal P_0 of device #D4 does not necessarily indicate stronger microscopic parasitic heating, since it scales directly with the assumed ΣΩ. The directly constrained quantity, $P_0/(\Sigma\Omega) = T_{e,sat}^5 - T_{p,min}^5$, is 9.6×10^{-8} K^5 for device #D3 and 1.5×10^{-8} K^5 for device #D4, indicating weaker normalized overheating in device #D4. The larger inferred P_0 may therefore reflect a thermally active Au volume smaller than its nominal value, possibly owing to finite Au/Al interfacial thermal resistance associated with residual oxidation or imperfect

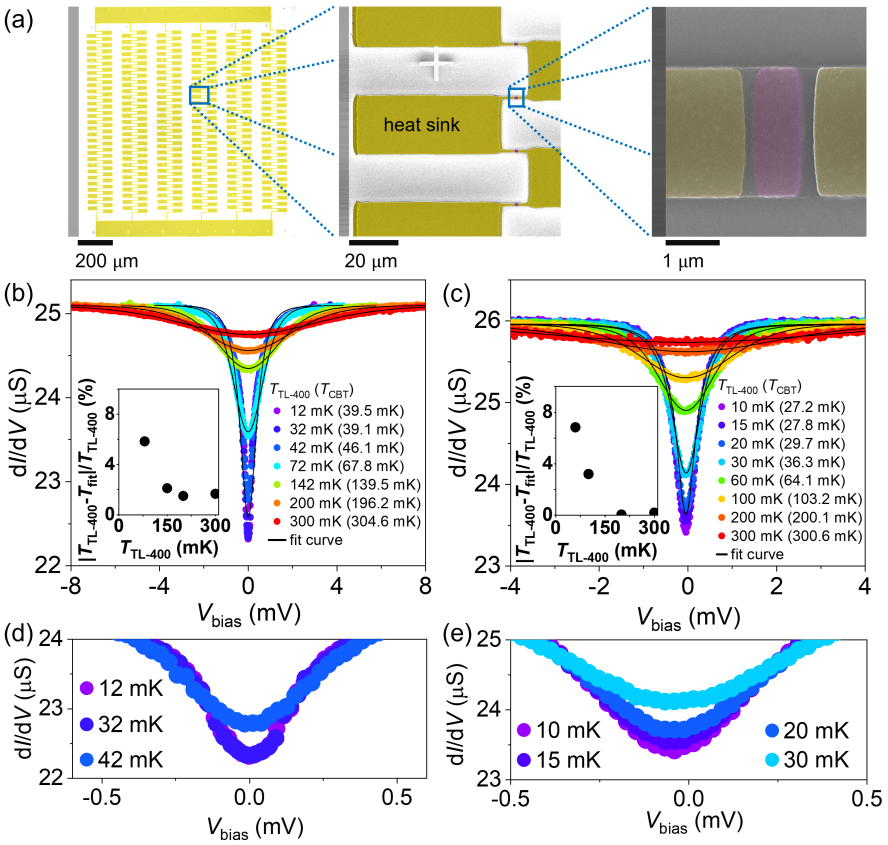


Fig. 4. Thermalization-optimized CBT devices. (a) False-color image of a CBT device with local metallic heat sinks integrated near the tunnel junctions. Gold and pink regions indicate the metallic electrodes/heat sinks and the junction area, respectively. (b, c) Differential conductance curves of devices #D3 and #D4 measured at different temperatures. Solid lines are full master-equation numerical fits. The inset in each panel shows the relative difference between the CBT-fitted temperature and the TL-400 dilution-refrigerator thermometer reading. (d, e) Magnified views of the low-temperature saturation regime in panels (b) and (c), respectively.

contact. Further optimization of the Al surface preparation and Au deposition is therefore needed to minimize this interfacial bottleneck and fully exploit the Au thermalization pads.

These results further indicate that wide-range CBT thermometry is most effectively achieved by combining multiple CBT devices optimized for different temperature intervals. Devices with larger charging energies exhibit higher thermometric sensitivity at elevated temperatures. However, as the temperature decreases, the increasing blockade parameter $u_N = E_C/k_BT$ makes the conductance line shape more sensitive to junction nonuniformity, thereby degrading the accuracy of temperature extraction. In contrast, devices with smaller charging energies are better suited for operation at lower temperatures, but they require higher junction uniformity, more efficient electron thermalization, and a lower-noise measurement environment. Moreover, the corresponding conductance dip becomes progressively shallower at elevated temperatures, eventually limiting reliable temperature calibration. Consequently, the practical design of CBT sensors requires a careful optimization of the junction capacitance, array geometry, and thermalization structure according to the target temperature range.

The temperature-calibration results of all fabricated devices are summarized in Fig. 5. Notably, the complementary characteristics of devices #D1 and #D4 enable CBT thermometry over a wide temperature range from approximately 30 mK to 3 K, spanning the operating regimes of both dilution-refrigerators and ^{3}He cryostats.

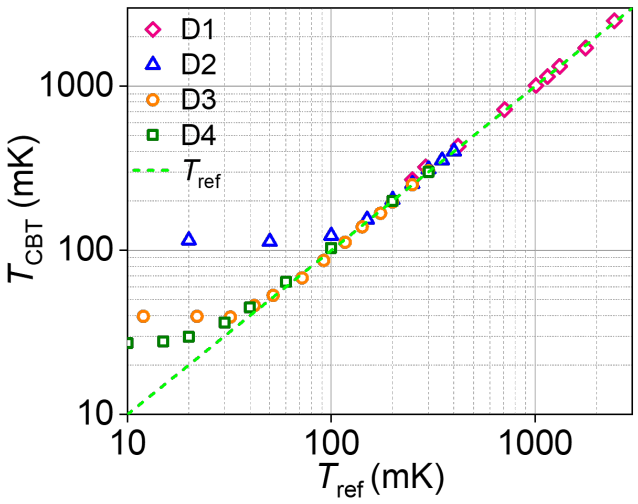


Fig. 5. The calibrated temperature responses of all fabricated devices. Here T_{ref} denotes the reference thermometer temperature of either the ^{3}He cryostat or the TL-400 dilution refrigerator. Devices #D1 and #D4 together provide electron thermometry over a broad range from approximately 30 mK to 3 K, bridging the dilution-refrigerator and ^{3}He temperature regimes.

4. Conclusion

We have developed and characterized $Al - Al_2O_3 - Al$ Coulomb blockade thermometers based on multi-junction tunnel-junction arrays. By employing MMA/PMMA bilayer electron-beam lithography, double-angle shadow evaporation, and *in situ* oxidation, highly reproducible tunnel junctions with well-controlled resistances were fabricated. The fabricated devices exhibit pronounced Coulomb-blockade conductance dips, whose temperature-dependent depths and widths are in good agreement with CBT theory. The multi-junction-array architecture effectively enhances the characteristic voltage scale and the signal-to-noise ratio of the thermometric response, while maintaining reliable operation in magnetic fields up to 10 T after the superconductivity of the Al electrodes is fully suppressed. Furthermore, by increasing the tunnel-junction area and incorporating large-volume on-chip Au thermalization electrodes, electron overheating at millikelvin temperatures is significantly suppressed, extending the thermometric range of the CBT down to approximately 30 mK.

These results demonstrate a practical route toward wide-range, magnetic-field-compatible on-chip electron thermometry for mesoscopic devices, superconducting circuits, and quantum-material devices operating in the millikelvin regime. Further optimization of thermalization, electrical filtering, and low-noise measurement circuitry is expected to extend the accessible temperature range to even lower temperatures, providing a robust platform for high-precision electron thermometry in ultralow-temperature experiments and cryogenic metrology.

Acknowledgments

This work is supported by the National Basic Research Program of China from the Ministry of Science and Technology (MOST) under grant Nos. 2022YFA1602803 and 2023YFA1607400, the National Natural Science Foundation of China under grant No. 12574060, the Synergetic Extreme Condition User Facility, and the Innovation Program for Quantum Science and Technology under Grant No. 2021ZD0302600.

References

[1] Pobell F 2007 *Matter and methods at low temperatures* vol 2 (Springer)

[2] White G K and Meeson P J 2002 *Experimental techniques in low-temperature physics* (Oxford University Press)

[3] Enss C and Hunklinger S 2005 *Low-temperature physics* (Springer)

[4] Giazotto F, Heikkilä T T, Luukanen A, Savin A M and Pekola J P 2006 *Rev. Mod. Phys.* **78**(1) 217–274

[5] Pekola J P, Hirvi K P, Kauppinen J P and Paalanen M A 1994 *Phys. Rev. Lett.* **73**(21) 2903–2906

[6] Hahtela O, Mykkänen E, Kemppinen A, Meschke M, Prunnila M, Gunnarsson D, Roschier L, Penttilä J and Pekola J 2016 *Metrologia* **54** 69

[7] Bradley D I, George R E, Gunnarsson D, Haley R P, Heikkinen H, Pashkin Y A, Penttilä J, Prance J R, Prunnila M, Roschier L *et al.* 2016 *Nat. Commun.* **7** 10455

[8] Meschke M, Kemppinen A and Pekola J P 2016 *Philos. Trans. R. Soc. A* **374** 20150052

[9] Hirvi K P, Kauppinen J P, Korotkov A N, Paalanen M A and Pekola J P 1995 *Appl. Phys. Lett.* **67** 2096–2098

[10] Farhangfar S, Hirvi K, Kauppinen J, Pekola J, Toppari J, Averin D and Korotkov A 1997 *J. Low Temp. Phys.* **108** 191–215

[11] Blanchet F, Chang Y C, Karimi B, Peltonen J T and Pekola J P 2022 *Phys. Rev. Appl.* **17**(1) L011003

[12] Samani M, Scheller C P, Sedeh O S, Zumbühl D M, Yurttagül N, Grigoras K, Gunnarsson D, Prunnila M, Jones A T, Prance J R and Haley R P 2022 *Phys. Rev. Res.* **4**(3) 033225

[13] Cole M C, Pelly M T, Topping C V, Reindl T, Waizmann U, Weis J and Rost A W 2025 *Rev. Sci. Instrum.* **96** 073903

[14] Wellstood F C, Urbina C and Clarke J 1994 *Phys. Rev. B* **49**(9) 5942–5955

[15] Palma M, Scheller C P, Maradan D, Feshchenko A V, Meschke M and Zumbühl D M 2017 *Appl. Phys. Lett.* **111** 253105

[16] Sarsby M, Yurttagül N and Geresdi A 2020 *Nat. Commun.* **11** 1492

[17] Autti S, Bettsworth F C, Grigoras K, Gunnarsson D, Haley R P, Jones A T, Pashkin Y A, Prance J R, Prunnila M, Thompson M D and Zmeev D E 2023 *Phys. Rev. Lett.* **131**(7) 077001

[18] Feshchenko A, Meschke M, Gunnarsson D, Prunnila M, Roschier L, Penttilä J and Pekola J 2013 *J. Low Temp. Phys.* **173** 36–44

[19] Averin D and Likharev K 1991 Chapter 6 - Single Electronics: A Correlated Transfer of Single Electrons and Cooper Pairs in Systems of Small Tunnel Junctions *Mesoscopic Phenomena in Solids* (*Modern Problems in Condensed Matter Sciences* vol 30) ed ALTSHULER B, LEE P and WEBB R (Elsevier) pp 173–271

[20] Devoret M H and Grabert H 1992 *Introduction to Single Charge Tunneling* (Springer US) pp 1–19

[21] Kauppinen J P and Pekola J P 1996 *Phys. Rev. B* **54**(12) R8353(R)–R8356(R)

[22] Meschke M, Pekola J, Gay F, Rapp R and Godfrin H 2004 *J. Low Temp. Phys.* **134** 1119–1143

[23] Dolan G J 1977 *Appl. Phys. Lett.* **31** 337–339

[24] Yurttagül N, Sarsby M and Geresdi A 2021 *J. Low Temp. Phys.* **204** 143–162

[25] Pekola J P, Taskinen L J and Farhangfar S 2000 *Appl. Phys. Lett.* **76** 3747–3749

[26] Pekola J P, Praks E, Yurttagül N and Karimi B 2022 *Metrologia* **59** 045009

[27] Hahtela O M, Meschke M, Savin A, Gunnarsson D, Prunnila M, Penttilä J S, Roschier L, Heinonen M, Manninen A and Pekola J P 2013 *AIP Conf. Proc.* **1552** 142–147

[28] Bradley D, Guénault A, Gunnarsson D, Haley R, Holt S, Jones A, Pashkin Y A, Penttilä J, Prance J, Prunnila M *et al.* 2017 *Sci. Rep.* **7** 45566

[29] Yurttagül N, Sarsby M and Geresdi A 2019 *Phys. Rev. Appl.* **12**(1) 011005